Tubular Carbon Nitride with Hierarchical Network: Localized Charge Carrier Generation and Reduced Charge Recombination for High-Performance Photocatalysis of H_2 and H_2O_2 Production

Xue Yu, Chengwei Hu, Danni Hao, Gen Liu, Rui Xu, Xiaodong Zhu, Xi Yu, Yanqing Ma, and Lei Ma**

Polymeric carbon nitride (PCN), as an appealing metal-free and low-cost photocatalyst for solar-to-fuel conversion, is still suffering from insufficient light-harvesting efficiency and short excited state lifetime of electron–hole pairs. Herein, a 3D hierarchical network of carbon nitride tubes (NCNT) with intercrossing few-layer tubes of uniform diameter, synthesized by a synergistic strategy of tailoring the chemical and hydrogen bond, is reported. This hollow network structure facilitates the internal light reflection, thus promoting the light-induced electron–hole pair generation. Moreover, the few-layer NCNT with nitrogen defects effectively decreases the undesired electron–hole recombination. These advantages are disclosed by experimental spectra and finite difference time domain (FDTD) simulations and density functional theory (DFT) calculations. Impressively, the optimized NCNT exhibits almost 32 times the photocatalytic hydrogen evolution ability (8.6 mmol h^{-1} g^{-1}) and 4 times (485.7 μmol h^{-1} g^{-1}) the hydrogen peroxide production of those of bulk PCN, respectively. This work provides a new strategy to construct a hierarchical nanostructure of a high-performance carbon nitride photocatalyst through enhancing the solar-light capture and conversion.

1. Introduction

Since the first report in the late 2010s, polymeric carbon nitride (PCN) has long been recognized as an attractive nonmetal photocatalyst for water splitting and artificial photosynthesis because of its advantages of low cost, high chemical stability, and a concise synthetic process.[1–4] However, the limited visible light absorption and short excited state lifetime of charge carriers are still the two main barricades for the practical applications of PCN.[5,6]

Due to the large specific surface area and therefore potentially abundant exposed active sites in the catalytic process,[7] as well as the theoretically much shorter diffusion path for photogenerated electrons and holes from the bulk to the surface, many researchers have endeavored to construct an ultrathin structure for photocatalysis.[8–11] Especially, ultrathin, even atomically thin nanosheets of PCN exhibit a superior photocatalytic H_2 evolution rate than bulk PCN.[12,13] However, ultrathin PCN unavoidably suffers from low visible light absorption because of an enlarged bandgap by the quantum size effect.[14] Heteroatom doping, introducing functional groups, and compounding with other semiconductors are often used as additional strategies to improve the light absorption.[15–18] But these additional modification processes are complicated and hard to control. In addition, they have a high possibility of introducing a large amount of unwanted recombination/trap centers for electron–hole pairs and eventually may contrarily lead to the deterioration of the photocatalytic performance.

The first step of photocatalysis is the generation of exited charges in the catalyst by light absorption. Designing photon traveling "channels" in a photocatalyst by morphology optimization is an effective strategy for promoting the light harvest and interactions of light with the catalyst to enhance the catalytic performance.[19,20] Especially, for construction of a hierarchical network structure, multiple light-scattering effects inside the pores and channels can significantly increase the light path and residence time further to improve light absorption.[21–24] There have been some reported attempts on trying to improve the utilization

---

X. Yu, C. Hu, Dr. D. Hao, G. Liu, Dr. R. Xu, Dr. X. Zhu, Dr. Y. Ma, Prof. L. Ma
Tianjin International Center for Nanoparticles and Nanosystems
Tianjin University
Tianjin 300072, P. R. China
E-mail: mayanqing@tju.edu.cn; lei.ma@tju.edu.cn

Dr. Y. Ma
State Key Laboratory of Precision Measuring Technology and Instruments
Tianjin University
Tianjin 300072, P. R. China

Prof. X. Yu
Tianjin Key Laboratory of Molecular Optoelectronic Sciences
Department of Chemistry
School of Science
Tianjin University & Collaborative Innovation Center of Chemical Science and Engineering (Tianjin)
Tianjin 300072, P. R. China

The ORCID identification number(s) for the author(s) of this article can be found under https://doi.org/10.1002/solr.202000827.

DOI: 10.1002/solr.202000827

of captured light by building a 3D PCN network assembled of nanorods, rings, or seaweed-like units.[25–27] However, it turned out that the photocatalysis efficiency was only improved marginally due to the serious recombination of charge carriers because of the largely shortened diffusion path of ions and electrons, although the light absorption of the whole system was dramatically enhanced. Assembling ultrathin nanotubes to a 3D structure can potentially resolve the aforementioned problems, with much more structure-tuning flexibility and higher light absorption efficiency. In addition, the long-range atomic arrangement can be easily tuned, and the defects introduced in the material also can effectively broaden the range of light absorption.[28,29] Therefore, from the perspective of photochemistry and photophysics, morphology control is an alternative route to improve the light absorption and facilitate photogenerated electron–hole utilization for high-performance PCN catalysis, which is to be well explored.[30]

Herein, a 3D network of carbon nitride tubes (NCNT) was synthesized through a facile method based on a synergistic route of glycol/nitric acid–mediated molecular tailoring and assembling followed by thermal polymerization. The obtained NCNT exhibits a hierarchical structure, which consists of intercrossing few-layer (thin to less than 4 nm) tubes with a uniform diameter of 600 nm. Special nitrogen defects are formed when assembled to the hierarchical network. The NCNT displays ≈2.1 times higher light absorption intensity than the bulk one and a largely extended light absorption range and progressive charge separation. Finite element analysis based Lumerical simulation of the excited optical field confirms the localized light-field enhancement, attributed to the increment of the photon utilization. DFT calculations further reveal that the nitrogen defect–tailored electron structure enlarges its light absorption range. Such a design of NCNT significantly promotes the photocatalytic hydrogen evolution ability (8.6 mmol h^{-1} g^{-1}) and hydrogen peroxide production (485.7 μmol h^{-1} g^{-1}), which are as high as those of bulk PCN and are superior values for pure PCN. Furthermore, this work also provides a general morphology control strategy to solve the photon absorption and charge carrier separation problems simultaneously for carbon nitride application in solar energy capture and conversion.

2. Results and Discussion

2.1. The Synthetic Strategy of 3D Tubular Carbon Nitride Network

The self-assembled tubular carbon nitride network can be achieved by the simple two-step approach shown in **Figure 1**. Briefly, the supramolecular structure consists of melamine and trithiocyanuric acid, assembled via forming NH/NH_2 and SH/NH_2 hydrogen bond groups.[31] The layered microrod supramolecular precursors are obtained by inserting nitric acid (Figures S1 and S2, Supporting Information), through which it is easy to break up the in-plane hydrogen bonds to decompose tri-*s*-triazine-based compounds into smaller molecules. The existence of the SH/NH_2 hydrogen bond groups can be used to tune the structure of the supramolecular precursor under nitric acid tailoring (Figure S3, Supporting Information).[31,32] The functional groups ($-NH_2$, $-SH$, $-OH$, etc.) enable the insertion of small molecules into the layered precursors.[12] It is found that inserting the glycol molecules facilitates few-layer nanosheet preparation (Figure S2, Supporting Information). Thus, tubular or nanobelt structural carbon nitride can be fabricated after thermal condensation, suggesting the insertion of glycol makes the exfoliation of carbon nitride rods easier (Figure S4, Supporting Information). When the calcination temperature is increased but below 300 °C, the size of the microrod is found to be smaller (Figure S5a,b, Supporting Information). In the polycondensation process in the range of 300–520 °C, the microsheets and microrods can transform to aggregated nanobelts (Figure S5c,d, Supporting Information). The exfoliated nanobelts can self-assemble into a tube-like network structure by thermal processing under a flowing N_2 atmosphere (Figure S4f, Supporting

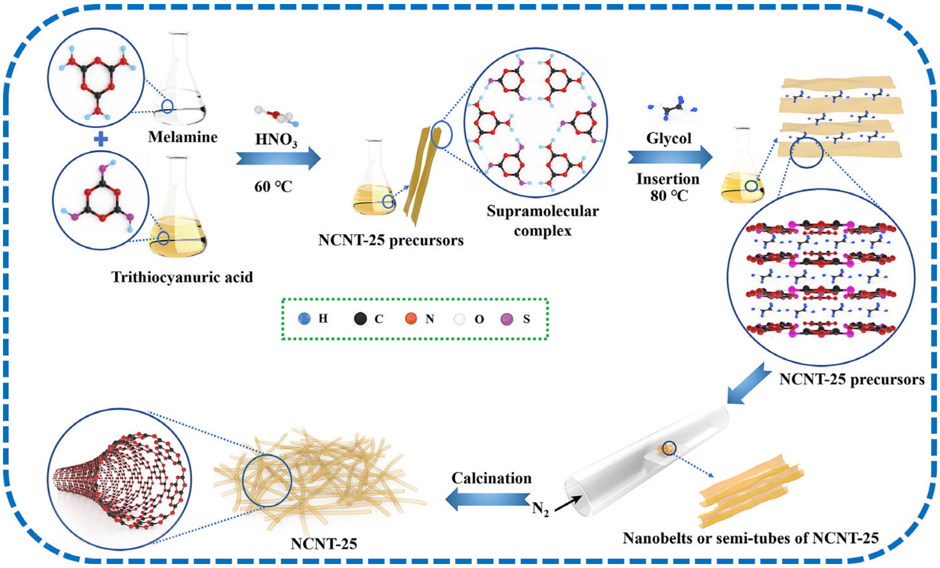

Figure 1. Schematic diagram of the synthetic process for few-layer tubular carbon nitride with hierarchical network structure.

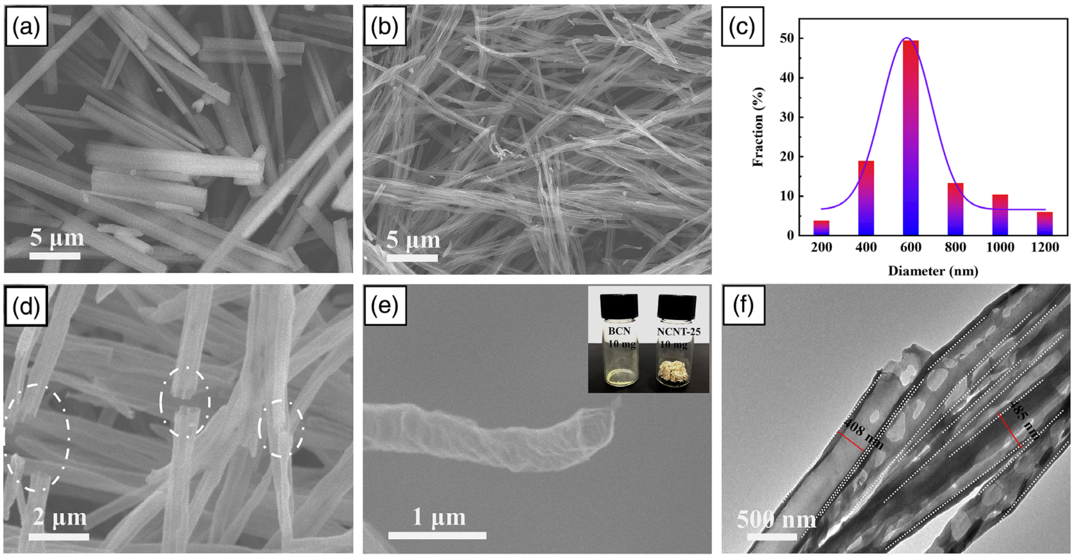

Figure 2. SEM images of the samples: a) precursors of NCNT-25 network, b) NCNT-25 network, and c) the corresponding diameter histogram of the NCNT-25 network. SEM images of the sample d) NCNT-25 and e) NCNT-25 nanotube and photograph of BCN and NCNT-25. f) TEM image of tubular NCNT-25.

Information) and finally produce the few-layer tubular 3D network carbon nitride. The formation of the hierarchical structure may be due to three main reasons: 1) The strong oxidation of nitric acid can open the structural hydrogen bonding between melon units;[33–35] 2) due to the high boiling point of glycol, the inserted glycol leads to a sufficient interlayer exfoliation;[12] and 3) the thermal process and cooling process can result in nanobelt curling due to the reduction of the high surface energy.[23,36] In addition, the solvents, the ratio of the mixture precursors, and the gas flow rate are also fine-tuned to optimize the configuration of the 3D network, and furthermore to investigate the thermal-induced condensation and chemical tailoring process (Figures S6–S8, Supporting Information).

2.2. Morphology and Structure Characterization

Here, all 3D tubular network carbon nitride (NCNT-25) samples are fabricated under a N_2 flow rate of 25 mL min^{-1} except for specific emphasis. The bulk carbon nitride (BCN) is prepared using a reference (Figure S9, Supporting Information).[12] The scanning electron microscopy (SEM) imaging shows that the supramolecular precursor for NCNT-25 possesses microsheet or microrod structure with diameter of ≈2–3 µm (**Figure 2**a). The 3D network structure with interconnected tubes and semi-tubes which have a large length-to-diameter ratio are shown in Figure 2b. The morphology of NCNT-25 is transformed from a microsheet to a thin crinkled tube with an average diameter of ≈600 nm (Figure S5d, Supporting Information, and Figure 2c). The thickness of NCNT-25 (the thickness of uncurled nanobelts) is ≈3.75 nm (Figure S10, Supporting Information). The NCNT-25 exhibits the characteristic of a tubular structure in Figure 2d,f. The energy disperse spectroscopy (EDS) mapping images evidence the uniform distribution of the elements C, N, and O in NCNT-25, as shown in Figure S11 and S12, Supporting Information. Moreover, compared with the BCN powder, the loose structure of NCNT leads to low density as shown in Figure 2e.

To analyze the in-plane and interlayer structure and texture of BCN and NCNT-25, XRD measurement results are shown in **Figure 3**a. Two major peaks can be observed from the spectrum of BCN at 13.3° and 27.4°, which correspond to the carbon nitride (100) and (002) orientation in the PDF #87-1526 card, respectively.[37] Compared with BCN, a much broader peak ranging from 26.2° to 27.4° is observed in the NCNT-25 sample. The interlayer spacing is increased, resulting in the few-layer structure of NCNT-25, which is coincident to the previous SEM-revealed structure. Meanwhile, no obvious (100) peak is observed, indicating the rapid decrease of in-plane order due to the forming of a curling tubular structure.[22,38,39] Furthermore, the strong bands at 1200–1700 cm^{-1} in the Fourier transform infrared spectra (FT-IR) absorption spectrum of BCN and NCNT-25 represent the stretching mode of the aromatic CN heterocycle (Figure 3b). The breathing mode of tri-*s*-triazine units in both the structure of BCN and that of NCNT-25 is indicated at the peak of 810 cm^{-1}. These peaks ambiguously indicate the intactness of the carbon nitride structure.[40] NCNT-25 shows wider peaks in the range of 2900–3500 cm^{-1} than BCN, indicating the higher abundance of surface N—H and O—H groups in NCNT-25 than in BCN.[22] Based on N_2 sorption isotherms of as-prepared samples and the Brunauer–Emmett–Teller equation, the specific surface area of NCNT-25 is calculated to be 96.11 $m^2\,g^{-1}$, which is higher than that of BCN (7.3 $m^2\,g^{-1}$). The N_2 absorption–desorption isotherm shows a typical IV isotherm with a type H3 hysteresis loop suggesting the presence of porous structure.[26,27,41] As shown in Figure 3c, the N_2 sorption of the NCNT-25 has a dramatic increase by an order of ≈3, indicating the heavily introduced pores and volume with the unique structure of this 3D network, and their size distribution is shown in Figure 3c (inset). It also

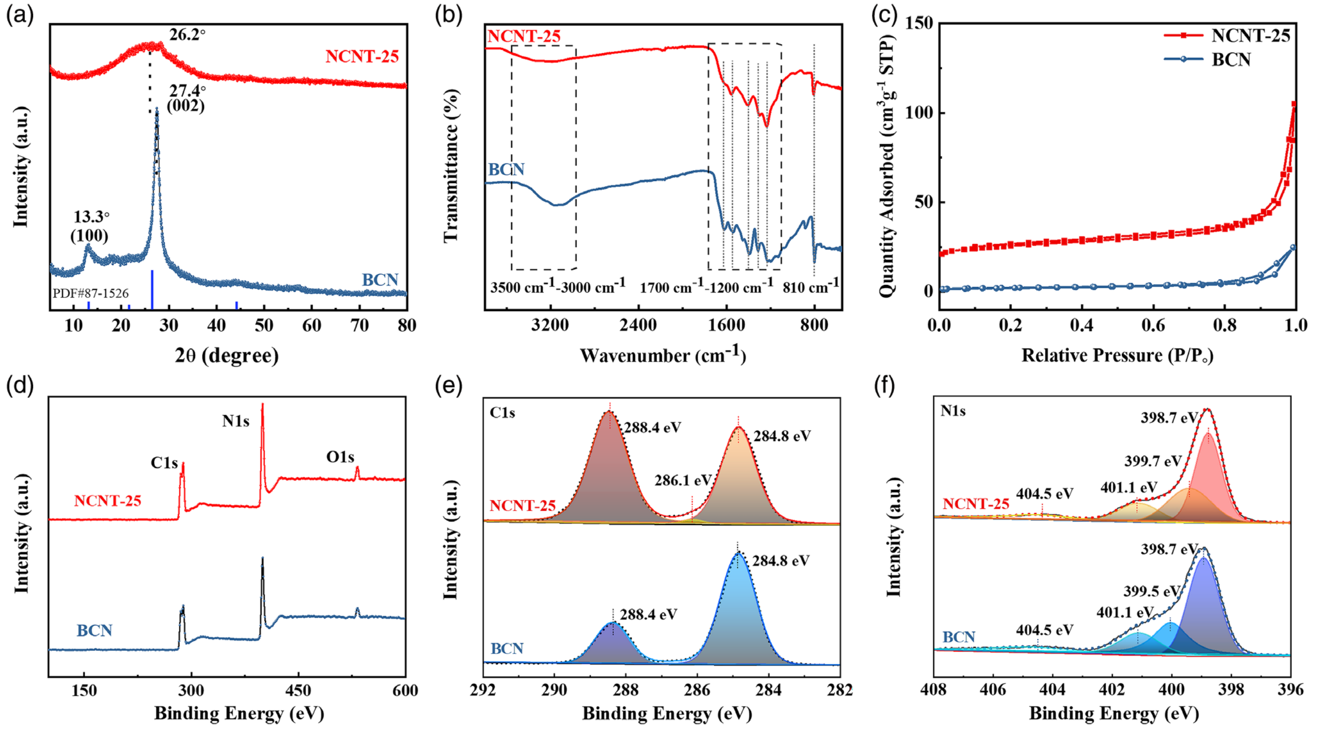

Figure 3. a) XRD patterns, b) FT-IR spectra, c) nitrogen isothermal adsorption–desorption curves (pore volume distribution inset), d) XPS survey spectra, and e) C 1*s* and f) N 1*s* XPS spectra of NCNT-25 and BCN samples.

indicates that the pore volume of NCNT-25 is much larger ($0.157\,cm^3\,g^{-1}$) than that of the control sample ($0.028\,cm^3\,g^{-1}$). Moreover, it is worth noting that the pore structure in the 3D network potentially can be well exploited for fast ion transfer and photogenerated charge carriers in the photocatalytic reaction.[10,25,41]

As shown in Figure 3d,f, from the X-ray photoelectron spectroscopy (XPS) measurements of BCN and NCNT-25, it is found that C 1*s*, N 1*s*, and O 1*s* are the main featured peaks. Rather weak O 1*s* peaks presumably result from H_2O, carbon oxide adsorption and/or oxidation.[15] Compared to BCN, the C-to-N atom ratio on the surface of NCNT-25 increases from 0.783 to 1.304 (Table S2, Supporting Information), which implies the diminishing of nitrogen atoms in the 3D network structure during the pyrolysis.[12] In Figure 3e, C 1*s* splits into two peaks; they are the most commonly seen C peak at 284.8 eV and a N—C═N bond peak at 288.4 eV.[25] Also, a new peak at around 286.1 eV in the spectrum of NCNT-25 reflects the presence of $C—NH_x$ or C—O, which probably originates from the breaking of the N═C—N.[12,17,29,42] The high-resolution spectrum of N 1*s* (Figure 3f) reveals three major peaks corresponding to sp^2-hybridized N (C(C═N—C)) at ≈398.7 eV, tertiary N ($C(N—(C)_3)$) located at 399.7 eV, and amino functional groups (—NH or NH_2) at 401.1 eV both for NCNT-25 and BCN.[31] In addition, the area ratio of the peak between 399.7 and 398.7 eV increases from 0.332 of BCN to 0.478 of NCNT-25, indicating the positive correlation between the nitrogen loss and peak area at 398.7 eV.[9,12] To further verify the discussion about the nitrogen defects, the room-temperature ESR spectra provide evidence for NCNT-25, as shown in Figure S13, Supporting Information. Compared with BCN, the largely stronger spin intensity of NCNT-25 gives evidence for the promotion of the formation of unpaired electrons. This is probably because the nitrogen defects would leave extra electrons, which are redistributed to their nearest C atoms delocalized among the big π-bonds of the carbon nitride.[43,44] The N vacancies produced by the lost N atoms further act as trapping sites for photogenerated charge carriers, thus inhibiting their recombination.[10,28]

Moreover, the peak at $979.7\,cm^{-1}$ in the measured Raman spectra represents the breathing mode of the triazine ring in both BCN and NCNT-25. The intensity increase of this peak of NCNT-25 (Figure S14, Supporting Information) is much more than that of BCN, further proving the large differences of the N defect yielding rate, at C(C═N—C)) into the melon structure between them.[45] A very weak signal of the element sulfur (S) can be observed from both the XPS and EDS spectra (Table S2 and Figure S11 and S12, Supporting Information). It is because most of the sulfur turns to exhausted H_2S; it is evidenced by the foul smell released from the furnace after calcination and the dark brown precipitate in the solution of copper sulfate.[31]

2.3. Photoabsorption Properties

The pristine photoabsorption property of BCN could be altered because of the 3D network nanostructure assembled by tubes. The UV–vis diffuse reflectance spectrophotometer (DRS) of the as-obtained NCNT samples, BCN and fiber-like structure are investigated as shown in **Figure 4** and Figure S15 and

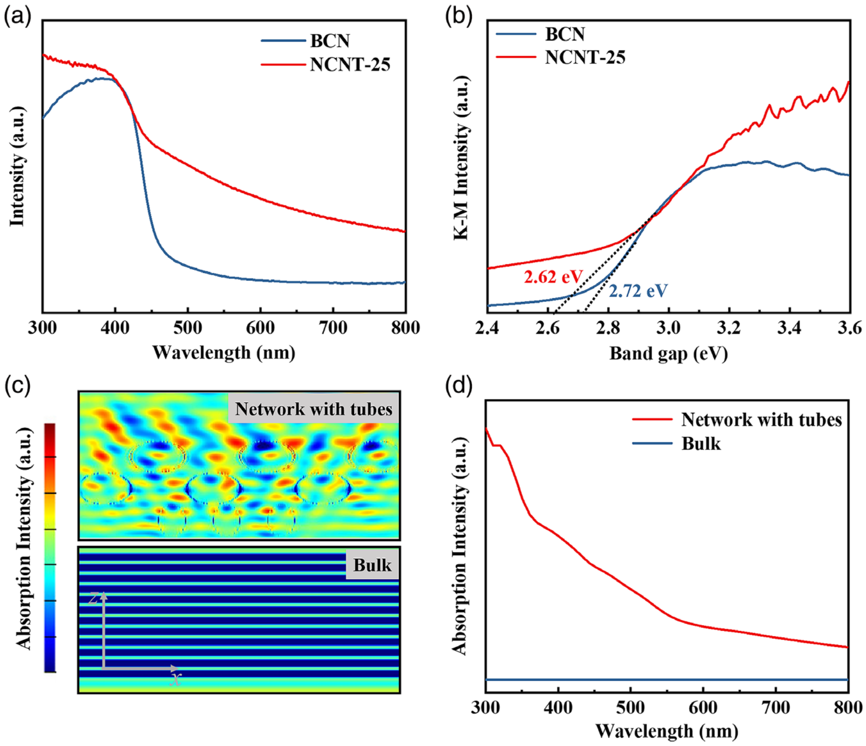

Figure 4. a) UV–vis absorption spectra and b) the corresponding bandgap energies of BCN and NCNT-25 samples; c) the distribution of the electrical field intensity and d) the diffused absorption intensity of the bulk structure and network structure.

S16, Supporting Information. In Figure 4a, a distinguishable redshift of the absorption edge of NCNT-25, compared with BCN, suggests the change of its intrinsic bandgap structure.[28] The bandgap energies (E_g) are derived from the Kubelka–Munk function and Tauc plots (by plotting $(\alpha h\nu)^{1/2}$ versus photon energy, where α is the absorption coefficient, h is the Planck constant, and ν is the light frequency),[46] which are ≈2.72 and 2.62 eV for BCN and NCNT-25, respectively (Figure 4b). The bandgap shrinking of NCNT-25 is mainly due to the existence of new electronic levels in the gap, which originate from the nitrogen defects and a trace amount of the sulfur atom–containing effect in the structure (Table S2, Supporting Information).[28,31]

Furthermore, the spectra show the enhancement of light absorption in the ranges 300–400 and 450–800 nm of NCNT-25. The intensified optical absorption can be interpreted as the enhanced localized photon absorption caused by the multistage scattering and reflection of the incident light in the hollow interlaced 3D tubular network structure.[25,28] Therefore, the light energy can be more adequately utilized in photocatalysis.

To further investigate the interaction of the incident photons with the NCNT,[20,30,46] as shown in Figure 4c,d, the simulation results of piles of tube-like and bulk carbon nitride, respectively, are presented. In carbon nitride hollow tube piles, the strong electric field is attributed to the inner multistage scatter and reflection of light happens at the tube–air interface, tube–tube interface, and inside the tube channels. Therefore, the light path distance and the light's residence time in the NCNT sample can be effectively increased. However, compared with the hierarchical tube-like network model, light propagates through the bulk structure with minor reflection. Moreover, with the increase of the layer number, the electric field enhances and distributes in a larger region, as shown in Figure S18, Supporting Information. In a word, the stacked hierarchical structure of the NCNT influences the optical characteristics of pristine carbon nitride. Inversely, due to the block morphology of BCN, light propagates through it with weak internal reflection and possesses a shorter light path than in the NCNT. Only two reflection interfaces can be observed at the air–BCN and BCN–air boundary. There is no obvious enhancement effect of the light intensity in the BCN samples.

2.4. Fast Charge Carrier Separation

Apart from that of the light trapping ability, systematic investigation of the generation, migration, and separation of charge carriers is critical to understand the photocatalytic procedure.[47,48] Steady-state and time-resolved photoluminescence (PL) are used to reveal the trapping, recombination, and separation of photoinduced charge carriers. As shown in **Figure 5**a, the PL intensity of NCNT-25 decreases drastically in comparison with that of BCN. It implies largely improved suppression of photogenerated electron–hole recombination in NCNT-25 compared to BCN. In addition, the redshift of the PL emission peak from 460 to 469 nm in NCNT-25 well reflects the change in its bandgap. As shown in Figure 5b,c, the measured PL of NCNT-25 shows a longer exponential decay time with an average lifetime of 11.93 ns than that of BCN (9.58 ns). The lifetime is contributed by three processes, namely, the nonradiative process (τ_1), radiative process (τ_2), and energy transfer process (τ_3).[25,41] The

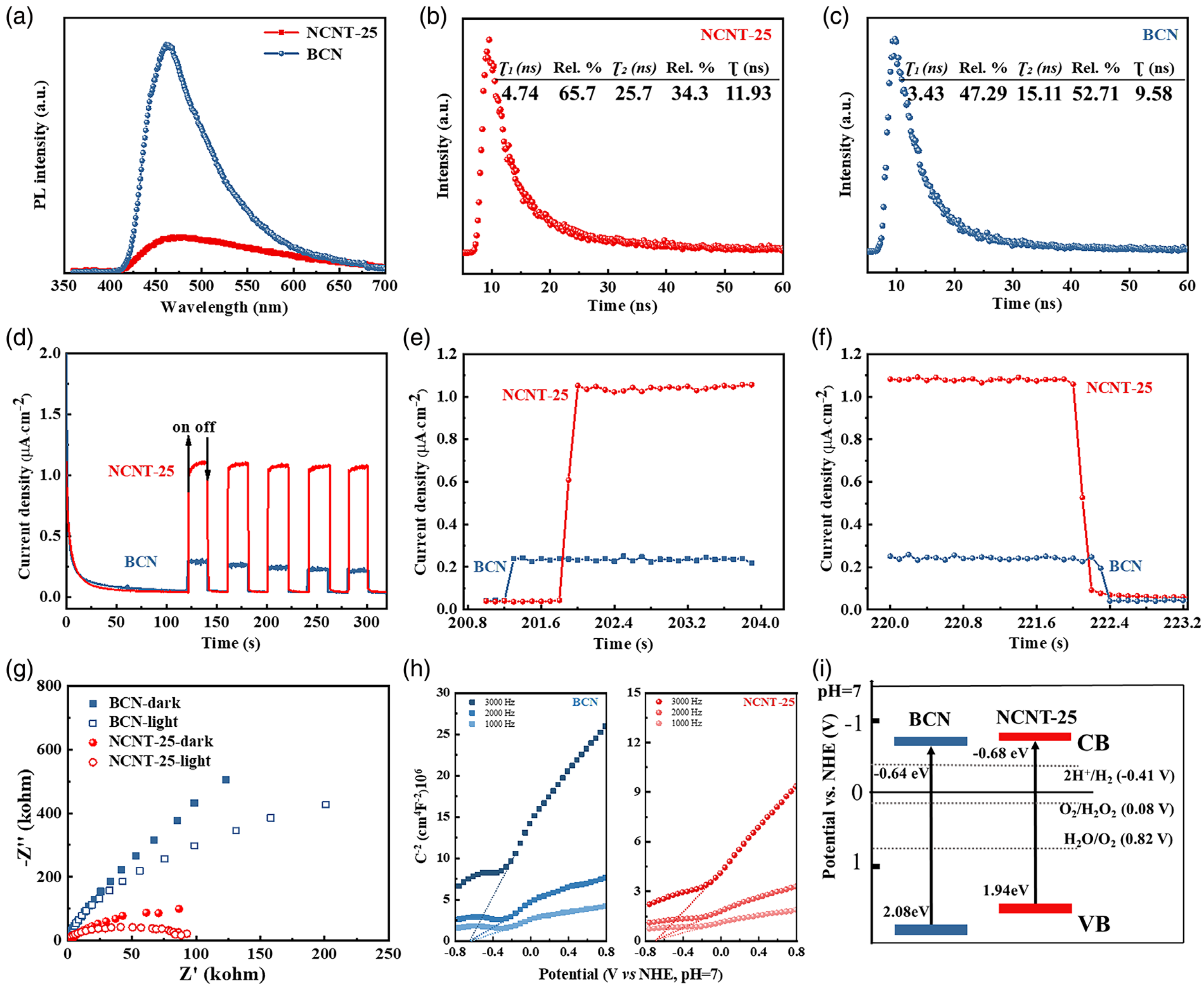

Figure 5. a) Steady-state PL spectra, b,c) time-resolved PL spectra, d) transient photocurrent response, e) rise-time dynamics of the transient photocurrent, f) decay-time dynamics of the transient photocurrent, g) EIS, h) Mott–Schottky plots with frequency of 1000, 2000, and 3000 Hz, and i) band structure diagram of BCN and NCNT-25.

radiative process (τ_2) is directly related to the separation of photogenerated electron–hole pairs. Fitting of the curves indicates that both τ_1 and τ_2 for NCNT-25 ($\tau_1 = 4.74$ ns, $\tau_2 = 25.70$ ns) exhibit a clear increase in comparison with those of BCN ($\tau_1 = 3.43$ ns, $\tau_2 = 15.11$ ns), suggesting that longer lifetime in NCNT provides more probabilities of photocarriers to be involved in the subsequent surface catalytic reaction.

The rise–decay dynamics of transient photoresponsive currents for NCNT and BCN were measured to provide direct information of the charge transfer efficiency.[30] As shown, the NCNT-25 photoelectrode displays a rather high photocurrent indicating the enhanced separation of charge carriers and efficient quenching of radiative recombination (Figure 5d). The faster increase (higher slope of the rise–decay curve) of the steady-state current furthermore is an evident enhancement of photogenerated electron and hole separation in NCNT (Figure 5e,f).

The electrochemical impedance spectroscopy (EIS) measurement displays a smaller diameter of semicircular in the Nyquist plot for NCNT-25 than that of BCN, which demonstrates that NCNT-25 has better electron transfer capability or higher electric conductivity (Figure 5g).[40] A similar tendency appears in the carrier density extracted from the slope of the measured Mott–Schottky curve (Figure 5h), implying that both the NCNT-25 and BCN are n-typed semiconductors and NCNT-25 possesses a higher carrier density compared to BCN.[49] These results exhibit significantly improved charge carrier mobility for few-layer tubular 3D network carbon nitride due to its thin-type nature, hierarchical structure, and impurity energy level.

The energy of the flatband E_{fb} of BCN and NCNT-25 was calculated from the measured Mott–Schottky curve in Figure 5i as −0.64 V (vs NHE) and −0.68 V (vs NHE), respectively, which furthermore can be used to calculate the location of the conduction band (CB).[15,19,23] Moreover, combined with the measured bandgap from the UV–vis spectra, their nominal valance band (VB) position was calculated as 2.08 and 1.94 eV, respectively.

In summary, the few-layer nanotube 3D networks can effectively improve the photon absorption, increase the mass transfer rate, and inhibit electron–hole recombination. Thus, an outstanding photocatalytic performance for NCNT among all the existing PCN-based photocatalysts is anticipated.

2.5. DFT Calculation for Electronic Property Analysis

DFT- based calculations were performed to further understand the influences of nitrogen defect sites on electronic structures of NCNT-25. The atomic structure models are shown in **Figure 6**a, b, which represent the pristine carbon nitride (M1-BCN) and carbon nitride with N vacancies (M2-NCNT), respectively. The type of intratriazine N vacancies is consistent with the results of NCNT-25 from the earlier XPS and Raman analysis. M2-NCNT shows a narrower bandgap (1.02 eV) than M1-BCN (1.2 eV) (Figure 6c,d). The decrease of the bandgap of M2-NCNT can explain the experimental redshift of the light-adsorption edge of NCNT-25. The narrowing of the bandgap is mainly attributed to the new band around the Fermi level.[50,51] The N vacancy–neighboring carbon in M2-NCNT owns a localized electronic density (Figure 6b, yellow color), indicating the improved electric conductivity resulting from the defect states. The partial density of states (PDOS) shows that the valence band is mainly dominated by the 2*p* orbital of N and the CB is mainly contributed by the 2*p* orbital of C and N. The Femi level of M1-BCN is close to the VB, whereas the Femi levels of M2-NCNT shift to the bottom of the CB, suggesting n-type systems. It implies that more electrons are available to involve the reduction reaction with photocatalysis. Furthermore, the calculated band edge shift between the BCN and NCNT, under the condition of NHE ($pH = 7$), perfectly reproduces the experimental measured ones (Figure S19, Supporting Information).[52]

2.6. Photocatalytic Performance and Photocatalysis Mechanism

The photocatalytic performance of the NCNT was evaluated through the H_2 evolution reaction (HER) in an aqueous medium with the addition of triethanolamine (TEOA) as a sacrificial electron donor and Pt as a cocatalyst. The H_2 evolution performance of the NCNT and that of BCN are shown in **Figure 7**. As expected, NCNT-25 shows the highest average amount of H_2 of 3.87 mmol in 3 h compared to others. It exhibits an average H_2 production rate of 1.29 mmol h^{-1}, which is ≈32 times higher than that of BCN (0.04 mmol h^{-1}). After 3 h of visible light ($\lambda > 420$ nm) and UV–vis light irradiation, NCNT-25 exhibits better performance of the H_2 evolution rate (≈8.6 and 24.93 mmol h^{-1} g^{-1}, respectively) (Figure 7b). The apparent quantum efficiency of NCNT-25 under 420 nm is 7.7% (Figure S20, Supporting Information), which is strong evidence of the maximization of photon gain and great photocatalytic performance. Moreover, the BMT without treatments of in-plane or/and interlayer hydrogen bond also shows lower performance of H_2 production, suggesting the importance of the thin and hierarchical network structure (Figure 7c). The 3D-structured carbon nitride rods and fibers also have superior HER performance compared to BCN, but it is still not comparable to that of the few-layer tubular NCNT-25 (Figure 7d).

Therefore, the structure of tubular 3D network carbon nitride provides enrichment of light adsorption ascribed to the holes and slits within the reticular conformation. In addition, the few-layer nanotubes can greatly reduce the diffusion path of charges and reactants from the interior to the surface. Furthermore, the network provides abundant active sites in the large surface area to improve the photocatalytic activity per unit area. The average HER rate versus specific surface area of NCNT-25 is 89.5 μmol h^{-1} m^{-2}, which is much higher than that of many other PCN photocatalysts (Table S3, Supporting Information). The increased surface area is probably not the main or necessary reason for the highly photocatalytic performance.[40,53] Furthermore, the cycling experiment of photocatalytic H_2 evolution and SEM images after reaction are executed, which carries out a relatively stable cyclic H_2 production (Figure S21, Supporting Information).

Moreover, considering the proper width and the energy of the bandgap, we also investigated the yielding rate of H_2O_2 applying

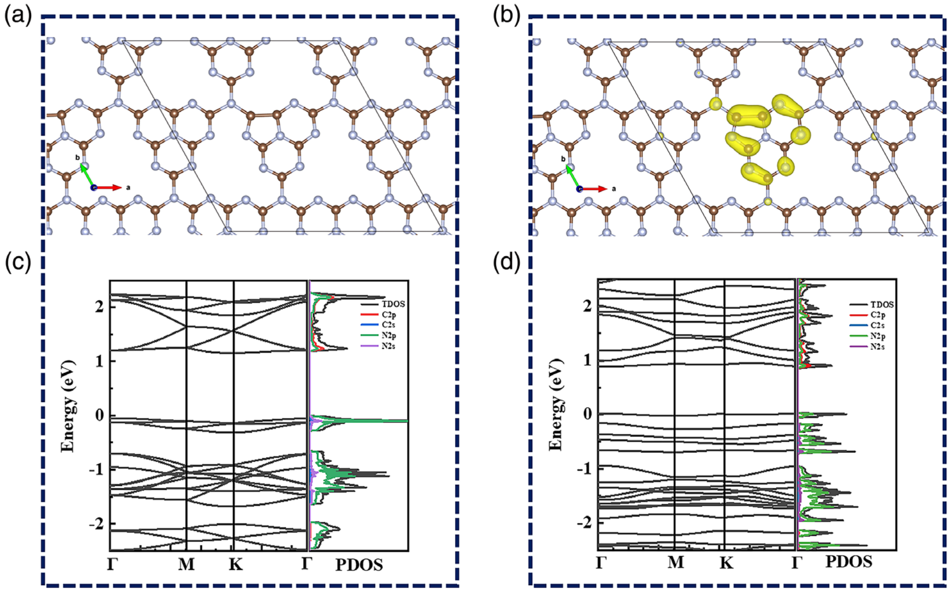

Figure 6. Structure models of a) M1-BCN, b) M2-NCNT with two-coordinated N vacancy (N1); calculated band structures, DOS, and PDOS for models of c) M1-BCN and d) M2-NCNT (brown balls: C atoms; white balls: N atoms).

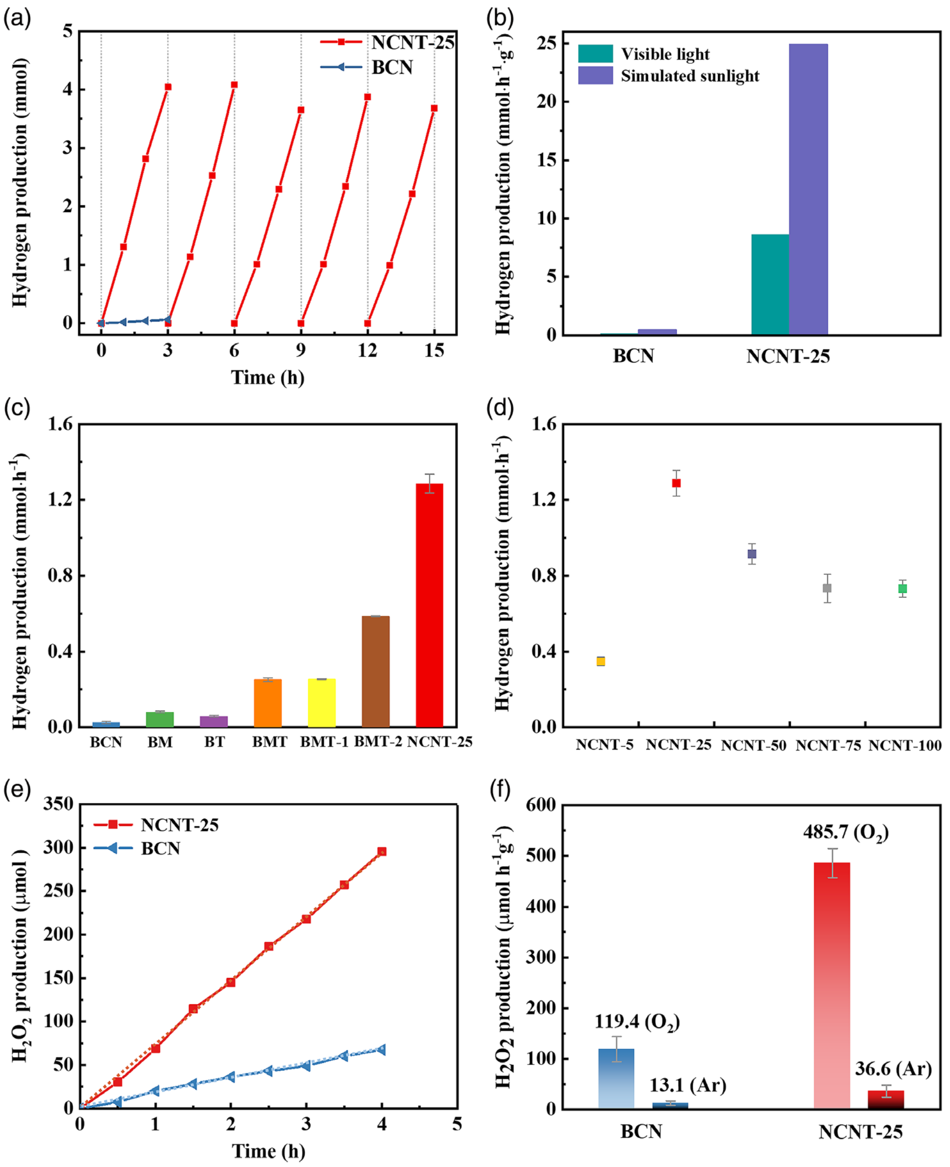

Figure 7. a) Cycling test of photocatalytic H_2 production, b) H_2 evolution rates of samples under visible light and UV–vis irradiation, c) comparison of the photocatalytic average H_2 production, d) photocatalytic performance of average H_2 production for NCNT samples with different gas flow rate prepared conditions, e) time-dependent evolution of H_2O_2 produced by BCN and NCNT-25, and f) photocatalytic performance of H_2O_2 production rate in contained O_2/ethanol/water system and Ar/ethanol/water system for BCN and NCNT-25 samples.

NCNT-25 and BCN as photocatalysts.[54] As shown in Figure 7e,f, the almost linear time-dependent yield indicates the extremely stable catalytic efficiency of both NCNT-25 and BCN, and also that of NCNT-25 is four times higher than that of BCN, which reaches ≈485.7 μmol h^{-1} g^{-1}. After five recycling tests (Figures S21 and S22, Supporting Information), the H_2O_2 production did not change too much (only decreasing by 7.6%), which indicates that the sample has relatively good stability. All the aforementioned reactions were performed in an O_2/ethanol/water system; when O_2 is replaced by Ar, less H_2O_2 is generated for both BCN and NCNT-25. This confirms that H_2O_2 originates from photocatalytic O_2 reduction.

The study provides a distinctive comparison between the tubular network structure and bulk structure of carbon nitride (**Figure 8**). Because the CB position of NCNT-25 well satisfies the requirement for reducing H^+ and O_2, it is intrinsically superior to BCN. On one hand, for the hydrogen production process, the excited holes remaining in the VB can interact with the sacrificial electron donor TEOA. The photoinduced electrons from the CB participate in the water reduction to produce H_2. On the other hand, for the hydrogen peroxide production, the excited holes remaining in the VB react with the ethanol to form acetaldehyde. The excited electrons react with O_2 to produce H_2O_2.

The largely enhanced photocatalytic ability of NCNT-25 compared with that of BCN can be attributed to the following factors: 1) The unique tubular 3D network structure dramatically increases the light absorption and prolongs the photon residence time due to the photon multiple reflection, thus much enriching

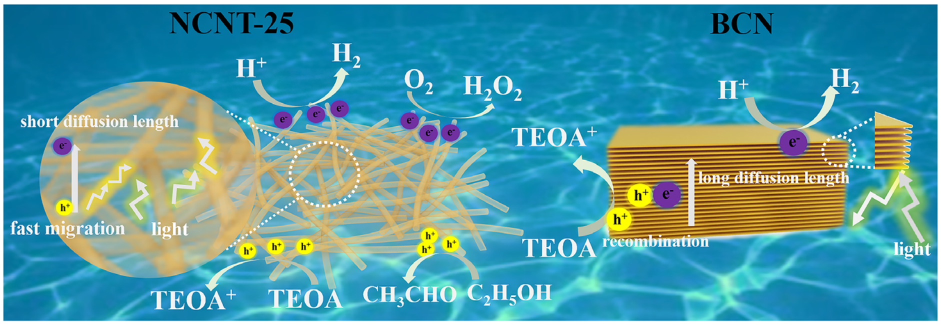

Figure 8. Photocatalytic mechanism in water of NCNT-25 and BCN samples.

the amount of excited carriers;[25,30] 2) the bandgap shrinking resulting from increased localized states expands the light absorption range;[17] 3) the increased defects/localized states induce the CB-TO-defect states' charge transfer processes, which favor the improved mobility and separation of photoinduced carriers;[12,31] and 4) the few-layer NCNT enables fast migration of electrons and reduces the diffusion path of electrons and holes.[13] The synergistic effect of all the aforementioned factors determines the photocatalytic performance of the 3D network of tubular carbon nitride.

3. Conclusion

In summary, a hierarchical network of carbon nitride tubes (NCNT) has been prepared by a novel strategy via a synergistic route of chemical tailoring and hydrogen bond modulation. The distinct structure of carbon nitride endows enhanced light absorption, an optimized band structure, and efficient charge carrier separation. The obtained NCNT could efficiently split water with a hydrogen production rate up to 8.6 mmol h^{-1} g^{-1} using Pt as a cocatalyst and also give enhanced hydrogen peroxide production with 485.7 μmol h^{-1} g^{-1}. The optical simulation (finite difference time domain (FDTD) solutions) evidences the effects of the intercrossing carbon nitride tubes on the enhancement of the localized photon absorption. These discoveries suggest that strategic design of the morphology of PCN can vastly improve both its optical and electrochemical properties, therefore largely enhancing the photocatalytic efficiency. We believe that this synergistic synthesis strategy of ultrathin carbon nitride with a 3D network structure certainly will vastly benefit the future structure design of photocatalysts for solar energy conversion and storage applications.

4. Experimental Section

Material Preparation: The NCNT precursor was prepared as follows. All the chemicals were purchased without further purification before being used in the material synthesis. Specifically, 0.455 g melamine and 0.225 g trithiocyanuric acid were dissolved in 15 mL glycol, respectively, at 60 °C. After stirring for 2 h, the melamine solution became transparent, and the trithiocyanuric acid became a uniform suspension. Then, the trithiocyanuric acid suspension was mixed with the melamine solution and stirred for 30 min, followed by dropwise addition of 0.2 M HNO_3 aqueous solution (60 mL) at a rate of 100 μL s^{-1} with 2 h stirring. Finally, the mixture was dried at 50 °C. The obtained precursors were mixed with 30 mL glycol at 80 °C and stirred for 2 h; after that, they were washed three times using ethanol.

The 3D network tubular carbon nitride (few-layer NCNT) was prepared as follows. In a typical fabrication process, the as-prepared mixture was treated in a tubing furnace heated quartz tube with a N_2 gas environment under the flow rate of 25 mL min^{-1}. After 30 min N_2 purging inside the quartz tube, first, the mixture was heated to 300 °C with a ramping rate of 2.5 °C min^{-1} and simmered for 1 h. It turned the mixture into a powder; then, it was continuously heated up to 520 °C with a ramping rate of 2.5 °C min^{-1} and kept at this temperature for another 2 h. Finally, the sample was cooled rapidly to 25 °C with a cooling rate of ≈60 °C min^{-1}. The network structure of the products is highly dependent on the gas flow rates and more detailed information is included in the Supporting Information. Other bulk structural samples named "BM," "BT," "BMT," "BMT-1," and "BMT-2" from different precursors were obtained, as listed in Table S1, Supporting Information.

The BCN was prepared as follows. As a contrast, bulk g-C_3N_4 powder was synthesized by calcinating the purchased melamine powder (5 g) at 500 °C for 4 h with a heating ramp of 2.5 °C min^{-1} in a muffle furnace.[12] The obtained product was ground to a fine powder labeled as "BCN."

Characterization: All the samples were characterized by powder X-ray diffraction (XRD) with Cu Kα radiation ($\lambda = 0.154$ nm), SEM (Hitachi SU3500), transmission electron microscopy (TEM, JEOL 2100), and atomic force microscopy (AFM, Park). An automatic Brunauer–Emmed–Teller (BET) analyzer (AUTOSORB IQ) was used to collect the BET surface areas (the samples were degassed at 200 °C for 8 h prior to the nitrogen adsorption measurements) and Raman spectra (532 nm excitation wavelength, Andor Solis); a UV–vis diffuse reflectance spectrophotometer (DRS, Hitachi U-3900) and Perkin-Elmer LS55 spectrophotometer for the steady-state photoluminescence (PL spectra with an excitation wavelength of 340 nm; and an Edinburgh FLSP980 fluorescence spectrometer with 465 nm as the detection wavelength for the measurement of the time-resolved PL spectra. High-resolution XPS was conducted with Al Kα radiation and an Ar^+ sputtering model (K-Alpha 1063, Thermo Fisher Scientific, England), and the electron spin resonance spectra (ESR, JES-FA200) and FT-IR spectra (Thermo Fisher Scientific) were also studied.

Supporting Information

Supporting Information is available from the Wiley Online Library or from the author.

Acknowledgements

This work was financially supported by the National Natural Science Foundation of China (No. 11774255) and the Key Project of Natural Science Foundation of Tianjin City (No. 17JCZDJC30100).

Conflict of Interest

The authors declare no conflict of interest.

Data Availability Statement

The data that supports the findings of this study are available in the supplementary material of this article.

Keywords

H_2 production, H_2O_2 production, hierarchical network morphology, nitrogen defects, tubular carbon nitride

Received: December 30, 2020
Revised: March 1, 2021

---

[1] X. Wang, K. Maeda, A. Thomas, K. Takanabe, X. Gang, J. M. Carlsson, K. Domen, M. Antonietti, *Nat. Mater.* **2009**, *8*, 76.
[2] X. Wang, F. Wang, Y. Sang, L. Hong, *Adv. Energy Mater.* **2017**, *7*, 1700473.
[3] L. Lei, D. Huang, C. Zhou, S. Chen, X. Yan, Z. Li, W. Wang, *Coordin. Chem. Rev.* **2020**, *408*, 213177.
[4] Y. Yang, X. Li, C. Zhou, W. Xiong, G. Zeng, D. Huang, C. Zhang, W. Wang, B. Song, X. Tang, X. Li, H. Guo, *Water Res.* **2020**, *184*, 116200.
[5] W.-J. Ong, L.-L. Tan, Y. H. Ng, S.-T. Yong, S.-P. Chai, *Chem. Rev.* **2016**, *116*, 7159.
[6] J. Fu, J. Yu, C. Jiang, B. Cheng, *Adv. Energy Mater.* **2018**, *8*, 1701503.
[7] H. Bian, Y. Ji, J. Yan, P. Li, L. Li, Y. Li, S. Liu, *Small* **2018**, *14*, 1703003.
[8] W. Che, W. Cheng, T. Yao, F. Tang, W. Liu, H. Su, Y. Huang, Q. Liu, J. Liu, F. Hu, *J. Am. Chem. Soc.* **2017**, *139*, 3021.
[9] Y. Li, M. Yang, Y. Xing, X. Liu, Y. Yang, X. Wang, S. Song, *Small* **2017**, *13*, 1701552.
[10] Q. Han, Z. Cheng, B. Wang, H. Zhang, L. Qu, *ACS Nano* **2018**, *12*, 5221.
[11] L. Lei, D. Huang, G. Zeng, M. Cheng, D. Jiang, C. Zhou, S. Chen, W. Wang, *Coordin. Chem. Rev.* **2019**, *399*, 213020.
[12] Y. Xiao, G. Tian, W. Li, Y. Xie, B. Jiang, C. Tian, D. Zhao, H. Fu, *J. Am. Chem. Soc.* **2019**, *141*, 2508.
[13] N. Meng, J. Ren, Y. Liu, Y. Huang, T. Petit, B. Zhang, *Energy Environ. Sci.* **2018**, *11*, 566.
[14] Y. Li, M. Yang, Y. Xing, X. Liu, Y. Yang, X. Wang, S. Song, *Small* **2017**, *13*, 1701552.
[15] B. Li, Y. Si, B.-X. Zhou, Q. Fang, Y.-Y. Li, W.-Q. Huang, W. Hu, A. Pan, X. Fan, G.-F. Huang, *ACS Appl. Mater. Interfaces* **2019**, *11*, 17341.
[16] M. Han, S. Lu, F. Qi, S. Zhu, H. Sun, B. Yang, *Sol. RRL* **2020**, *4*, 2070041.
[17] X. Zhao, Y. Zhang, X. Zhao, X. Wang, Y. Zhao, H. Tan, H. Zhu, W. Ho, H. Sun, Y. Li, *ACS Appl. Mater. Interfaces* **2019**, *11*, 27934.
[18] W. Wang, Q. Niu, G. Zeng, C. Zhang, D. Huang, B. Shao, C. Zhou, Y. Yang, Y. Liu, H. Guo, W. Xiong, L. Lei, S. Liu, H. Yi, S. Chen, X. Tang, *Appl. Catal., B* **2020**, *273*, 119051.
[19] M. Z. Rahman, P. C. Tapping, T. W. Kee, R. Smernik, N. Spooner, J. Moffatt, Y. Tang, K. Davey, S. Z. Qiao, *Adv. Funct. Mater.* **2017**, *27*, 1702384.
[20] Y. Li, Z. Ruan, Y. He, J. Li, K. Li, Y. Jiang, X. Xu, Y. Yuan, K. Lin, *Appl. Catal., B* **2018**, *236*, 64.
[21] H. Ou, P. Yang, L. Lin, M. Anpo, X. Wang, *Angew. Chem., Int. Ed.* **2017**, *56*, 10905.
[22] Q. Han, B. Wang, Y. Zhao, C. Hu, L. Qu, *Angew. Chem., Int. Ed.* **2015**, *54*, 11433.
[23] J. Fu, B. Zhu, C. Jiang, B. Cheng, W. You, J. Yu, *Small* **2017**, *13*, 1603938.
[24] D. He, C. Zhang, G. Zeng, Y. Yang, D. Huang, L. Wang, H. Wang, *Appl. Catal., B* **2019**, *258*, 117957.
[25] W. Luo, X. Chen, Z. Wei, D. Liu, W. Yao, Y. Zhu, *Appl. Catal., B* **2019**, *255*, 117761.
[26] W. Yu, T. Zhang, Z. Zhao, *Appl. Catal., B* **2020**, *278*, 119342.
[27] Y. Liu, X. Guo, Z. Chen, W. Zhang, Y. Wang, Y. Zheng, X. Tang, M. Zhang, Z. Peng, R. Li, Y. Huang, *Appl. Catal., B* **2020**, *266*, 118624.
[28] G. Ge, X. Guo, C. Song, Z. Zhao, *ACS Appl. Mater. Interfaces* **2018**, *10*, 18746.
[29] Y. Wang, D. Meng, X. Zhao, *Appl. Catal., B* **2020**, *273*, 119064.
[30] M. Rahman, J. Moffatt, N. Spooner, *Mater. Horiz.* **2018**, *5*, 553.
[31] H. Wang, Y. Bian, J. Hu, L. Dai, *Appl. Catal., B* **2018**, *238*, 592.
[32] Q. Fan, J. Liu, Y. Yu, S. Zuo, B. Li, *Appl. Surf. Sci.* **2017**, *391*, 360.
[33] M. Tahir, C. Cao, F.K. Butt, F. Idrees, N. Mahmood, Z. Ali, I. Aslam, M. Tanveer, M. Rizwan, T. Mahmood, *J. Mater. Chem. A* **2013**, *1*, 13949.
[34] J. Gao, Y. Zhou, Z. Li, S. Yan, N. Wang, Z. Zou, *Nanoscale* **2012**, *4*, 3687.
[35] Y. Kang, Y. Yang, L.C. Yin, X. Kang, L. Wang, G. Liu, H. M. Cheng, *Adv. Mater.* **2016**, *28*, 6471.
[36] S. Wang, C. Li, T. Wang, P. Zhang, A. Li, J. Gong, *J. Mater. Chem. A* **2014**, *2*, 2885.
[37] H. Ou, L. Lin, Y. Zheng, P. Yang, Y. Fang, X. Wang, *Adv. Mater.* **2017**, *29*, 1700008.
[38] Y. Wang, L. Li, Y. Wei, J. Xue, H. Chen, L. Ding, J. Caro, H. Wang, *Angew. Chem., Int. Ed.* **2017**, *56*, 8974.
[39] Y. Zhang, Z. Zhou, Y. Shen, Q. Zhou, J. Wang, A. Liu, S. Liu, Y. Zhang, *ACS Nano* **2016**, *10*, 9036.
[40] L. Cui, J. Song, A. F. McGuire, S. Kang, X. Fang, J. Wang, C. Yin, X. Li, Y. Wang, B. Cui, *ACS Nano* **2018**, *12*, 5551.
[41] B. Lin, H. An, X. Yan, T. Zhang, J. Wei, G. Yang, *Appl. Catal., B* **2017**, *210*, 173.
[42] H. Yu, R. Shi, Y. Zhao, T. Bian, Y. Zhao, C. Zhou, G. I. N. Waterhouse, L.-Z. Wu, C.-H. Tung, T. Zhang, *Adv. Mater.* **2017**, *29*, 1605148.
[43] L. Yang, J. Huang, L. Shi, L. Cao, Q. Yu, Y. Jie, J. Fei, H. Ouyang, J. Ye, *Appl. Catal., B* **2017**, *204*, 335.
[44] L. Shi, L. Yang, W. Zhou, Y. Liu, L. Yin, X. Hai, H. Song, J. Ye, *Small* **2018**, *14*, 1703142.
[45] H. Li, C. Jin, Z. Wang, Y. Liu, P. Wang, Z. Zheng, M.-H. Whangbo, L. Kou, Y. Li, Y. Dai, B. Huang, *Chem. Eng. J.* **2019**, *369*, 263.
[46] Y. Kang, Y. Yang, L. C. Yin, X. Kang, G. Liu, H. M. Cheng, *Adv. Mater.* **2015**, *27*, 4572.
[47] C. F. Fu, X. Wu, J. Yang, *Adv. Mater.* **2018**, *30*, 1802106.
[48] S. Chen, T. Takata, K. Domen, *Nat. Rev. Mater.* **2017**, *2*, 17050.
[49] U. Sim, J. Moon, J. An, J. H. Kang, S. E. Jerng, J. Moon, S.-P. Cho, B. H. Hong, K. T. Nam, *Energy Environ. Sci.* **2015**, *8*, 1329.
[50] Q. Tay, P. Kanhere, C. F. Ng, S. Chen, Z. Chen, *Chem. Mater.* **2015**, *27*, 4930.
[51] H. Liu, S. Ma, L. Shao, H. Liu, Q. Gao, B. Li, H. Fu, S. Fu, H. Ye, F. Zhao, J. Zhou, *Appl. Catal., B* **2020**, *261*, 118201.
[52] Y. Wang, Y. Tian, L. Yan, Z. Su, *J. Phys. Chem. C* **2018**, *122*, 7712.
[53] Y. Yu, W. Yan, X. Wang, P. Li, W. Gao, H. Zou, S. Wu, K. Ding, *Adv. Mater.* **2018**, *30*, 1705060.
[54] J. Lei, B. Chen, W. Lv, L. Zhou, L. Wang, Y. Liu, J. Zhang, *ACS Sustainable Chem. Eng.* **2019**, *7*, 16467.